AIAA 80-1379R

Propagation of Pulsed Laser Energy Through the Atmosphere

M. Autric,* J. P. Caressa,† Ph. Bournot,‡ D. Dufresne,‡ and M. Sarazin§
Institute of Fluid Mechanics, Marseille, France

An experimental investigation has been conducted to study pulsed laser energy propagation over long distance through the atmosphere. Typical gain switched pulse of the CO_2 cold cathode electron gun laser (160 J, 2.5 μs) shows an initial high-power spike (5.6×10^8 W, 50 ns FWHM) followed by a high-energy tail (130 J). The laser beam is focused by means of of a 5 X telescope outside the laboratory. Spatial and temporal distributions of intensity and energy density are measured in the breakdown area by burning of thermosensitive paper (envelope of the focused laser beam) and by use of calibrated Kalvar film (focal spot). Experimental determination of the air breakdown average threshold ($1\text{-}2\times10^8$ W/cm^2, 3-5 J/cm^2) leads to the conclusion that such a phenomenon is initiated on the spike of the pulse by $\geq$ 4-μm-diam aerosol particles. A particle optical counter is used for in situ measurements of aerosol distribution (axially scattering spectrometer probe, calibrated in the 0.5 $\mu m \leq d \leq 45$ μm range), to determine the number in the focal volume.

Introduction

NUMEROUS published experimental studies on the interaction between CO_2 laser beams and targets at intensity levels of $10^7\text{-}5\times10^8$ W/cm^2 have been conducted to measure the total impulse transferred to a surface by high-power 10.6 μm pulsed lasers (for laser propulsion, thermomechanical effects on target, etc.). During such intensity and fluence transport through a dusty and aerosol filled atmosphere, air breakdown is liable to occur.

It has been shown[1-11] theoretically and experimentally that the presence of these microscopic particles can lower the breakdown threshold, for 50 ns laser pulses, down to 0.1-0.02 times that of clean air. Basically, the breakdown threshold has been found to be especially sensitive to particle size, focal spot size, and laser-pulse length. The experimental results presented in this paper take into account diffraction of the annular apertured beam, spherical aberration phenomena induced by the focusing optical system, spatial and temporal energy density distributions in the focal spot, and atmospheric aerosol particle distribution found in the breakdown area in order to determne intensity and fluence threshold values necessary to cause air breakdown.

Experimental Apparatus

Laser Pulse

The CO_2 cold cathode electron gun type laser used during these experiments in an unstable oscillator configuration [a two-mirror unstable p-branch cavity ($L=2.65$ m, geometrical output coupling $\delta=0.57$)] displays a characteristic annular intensity distribution (external diameter $D=100$ mm, internal diameter $d=65$ mm). The typical gain switched pulse (160 J, 2.5 μs) of a 3-2-1 He-N_2-CO_2 mixture consists of an initial high power spike (5.6×10^8 W) with a rise time of 50 ns in the ramping portion and 50 ns full width at half maximum, followed by a high-energy low-power tail (130 J, 10^8 W, 2.5 μs). In Fig. 1b, the oscillograph shows the output pulse waveform measured by a photon drag detector.

Because of propagation losses (mirrors, telescope) the delivered pulse average characteristics measured near the focal plane are slightly different (see Table 1). The temporal development of the pulse does not change.

The temporal shape of each output pulse is monitored by a germanium photon-drag detector which blocks off the low percentage of energy reflected on the NaCl window L_1 (Fig. 1a).

An NaCl beam splitter L_2 is used to direct a fraction of the incident radiation onto a calorimeter and to control shot-to-shot energy variations (less than 10%). A set of calibrated attenuators (mylar) is used to study the phenomenon for variable incident energy. The experimental device is schematically represented in Fig. 2.

Table 1 Experimental conditions[a]

f, m	D, m	f/D	Δt, ns	W_{max}, W$\times10^8$	E, J
67.5	0.5	135	50	4.2	140[b]
158.5	0.5	317	50	3	150[c]
214	0.5	428	50	3	150[c]

[a] f = focal length; D = laser beam diameter on the exit pupil of the 5X telescope; $f/D=F$ number of the optical system; Δt = rise time of laser pulse; W_{max} = maximum power ($t=50$ ns); E = total incident energy in the focal zone. [b] $E/p=5.5$ kV$\times$cm$^{-1}\times$b^{-1}. [c] $E/p=6$ kV$\times$cm$^{-1}\times$b^{-1}.

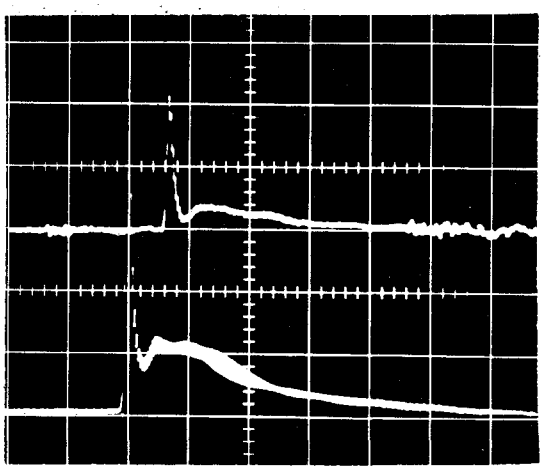

Fig. 1 Incident laser intensity variations (lower trace). The upper trace represents the laser test: 500 ns/division, 10^8 W/division.

Presented as Paper 80-1379 at the AIAA 13th Fluid and Plasma Dynamics Conference, Snowmass, Colo., July 14-16, 1980; submitted Sept. 18, 1980; revision received April 3, 1981.

*Research Scientist, Centre National de la Recherche Scientifique. Member AIAA.
†Research Scientist, Centre National de la Recherche Scientifique.
‡Maître-Assistant, University of Aix-Marseille II.
§Postdoctoral Fellow; presently at the University of Washington, Seattle, Wash.

Focusing Optical System

Field experiments were conducted by means of a two-mirror beam expander (5X telescope) with a "Cassegrain" configuration (parabolic mirror, $f=1$ m, $\phi=0.65$ m; hyperbolic mirror, $f=0.2$ m, $\phi=0.12$ m; $\epsilon=-1.127$). The focal length f may vary by translating the hyperbolic mirror along the optical axis. The position $f=160$ m (adaptation distance) is free from spherical aberrations; the intensity distribution in the focal plane is then given by diffraction theory.

Considering that the spherical aberrations induced by the telescope and that the nature of the diffraction limited annular beam interfere in the focal area (Fig. 3), it was decided to work on both sides of the adaptation distance ($f=67.5$, 158.5, and 214 m, $f/D=135$, 317, and 428). Careful alignment of the optical system allows almost complete elimination of off-axis aberrations: an He-Ne laser beam, simulating the CO_2 laser beam, permits observation of the effects of misalignment on the far-field distribution.

Experimental Results

The purpose of the experiment is to investigate the laser energy transport over long distances (breakdown threshold fluence and breakdown threshold intensity) and the influence of atmospheric aerosol particles on this phenomenon. The results presented here complete previously published results.[12,13]

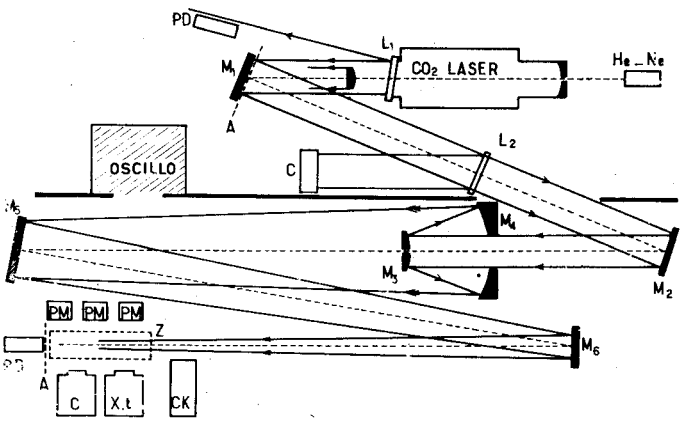

Fig. 2 Experimental apparatus: L_1, L_2—NaCl windows; PD—photon-drag detector; C—calorimeter; PM—photomultiplier; C′—camera; A—attenuators; He-Ne—6328 Å laser probe; X.t—streak camera; CK—particle optical counter; M_1,M_2,M_5,M_6—plane mirrors; M_3—hyperbolic mirror; M_4—parabolic mirror; z—breakdown region.

Spatial Intensity Distribution along the Beam

Intensity cross-sectional variations along the focused beam axis are measured by burning, with constant incident energy, light-blackened photographic paper sheets. Comparison of burn spots (each color change of the paper is considered as a burning step) allows qualitative determination of intensity distribution variations and the position of the plane with the best energy concentration (plane of best focus). This plane is then chosen for the study of spatial energy density distribution using Kalvar film.

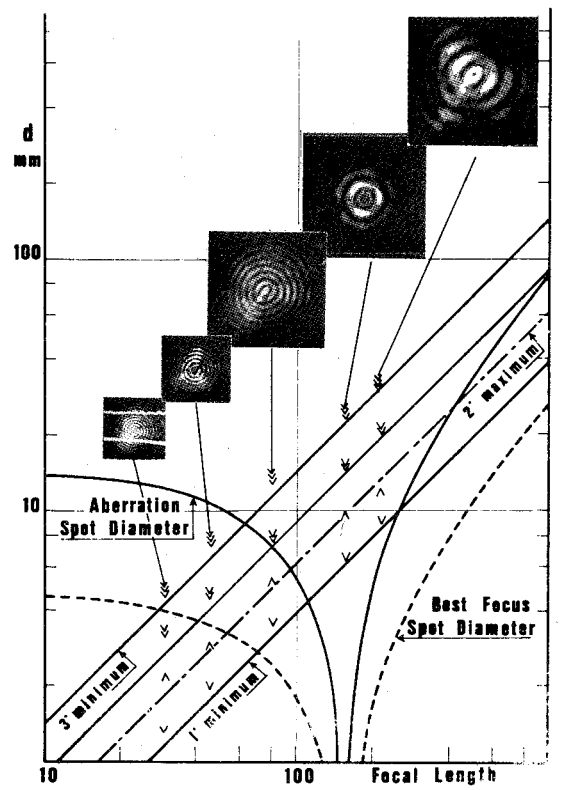

Fig. 3 Laser burn pattern compared with theoretical spot size for either spherical aberrations or far-field diffraction.

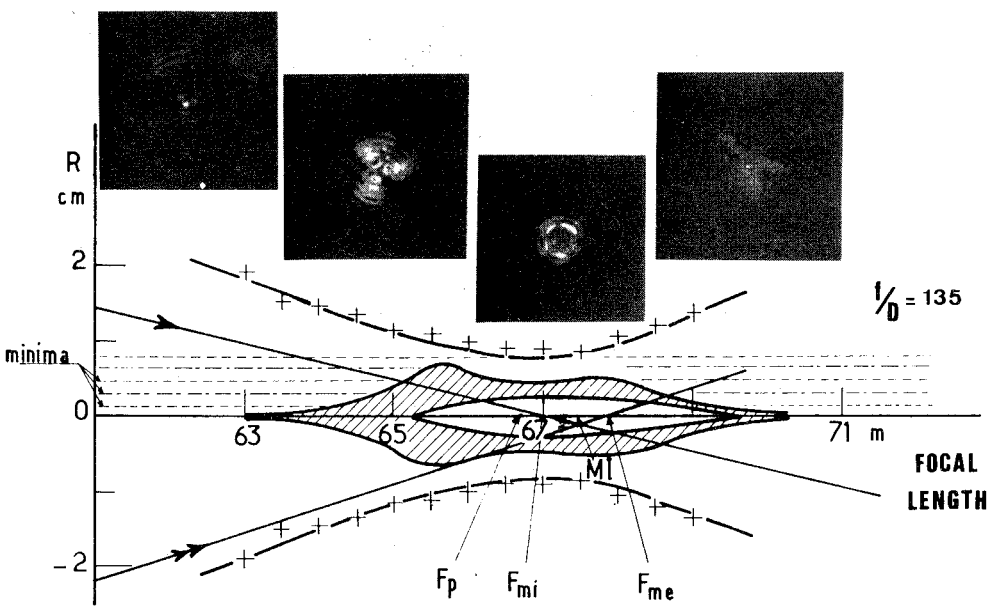

Fig. 4 Laser burn pattern associated to axial intensity contour diagram.

Table 2 Percentage of incident energy located in each diffraction ring for different experimental conditions

f/D	1-deg ring (center)	2-deg ring	3-deg ring	4-deg ring	5-deg ring	6-deg ring
135	15.7	19.5	21.9	22.6	13.1	7.1
317	17.9	24.1	24.4	24	9.6	...
428	17.5	35.4	34.9	12.3	...	...
...	40	31	20	8	1	0.1

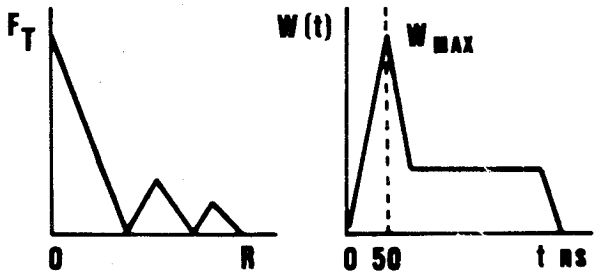

Fig. 5 Scheme of the diffraction ring-structure and laser pulse shape. F_T is the total fluence, $\Delta t = 50$ ns.

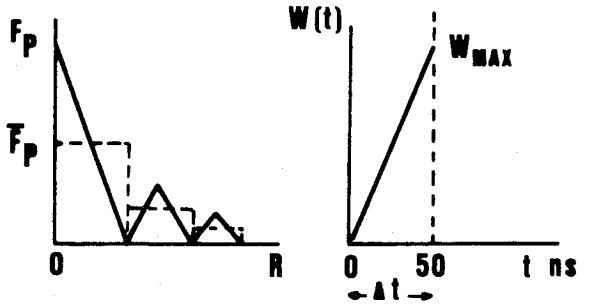

Fig. 6 Scheme of the diffraction ring-structure energy density distribution and the ramping portion of the spike. F_P is the peak fluence at $t = 50$ ns.

Figure 4 is an axial intensity contour diagram at $f/D = 135$. It shows the two marginal focuses (F_{mi} for the external edge and F_{me} for the external edge), the paraxial focus F_p, and the plane of best focus MI.

Energy Density Distribution in the Plane of Best Focus

Energy density distribution in a plane close to the plane of best focus is measured by means of calibrated Type-100 Kalvar film.[14,15]

This film consists of a transparent polyester base (mylar) coated with a 10-μm-thick thermoplastic resin which contains an ultraviolet (uv) sensitive compound—a diazonium salt. The film is first sensitized by exposure to uniform saturating uv light and the laser infrared (ir) radiation then selectively develops it. Used to estimate quantitatively the spatial energy density distribution in a laser beam (10 μm accuracy), this film can detect energy densities down to approximately 0.75 J/cm^2 and presents a damage threshold of about 3 J/cm^2. It is possible to cover the entire dynamic range of the laser spot energy by using several exposures with different attenuators.

The resulting density pattern is compared to the CO_2 beam pattern by means of a microdensitometer. The accuracy of the whole measurement depends upon uv pre-exposure level, time lapse between uv and ir exposures, initial temperature of the film and numerical aperture of the microdensitometer. Table 2 presents the ratio of total incident energy E_T located in each diffraction ring.

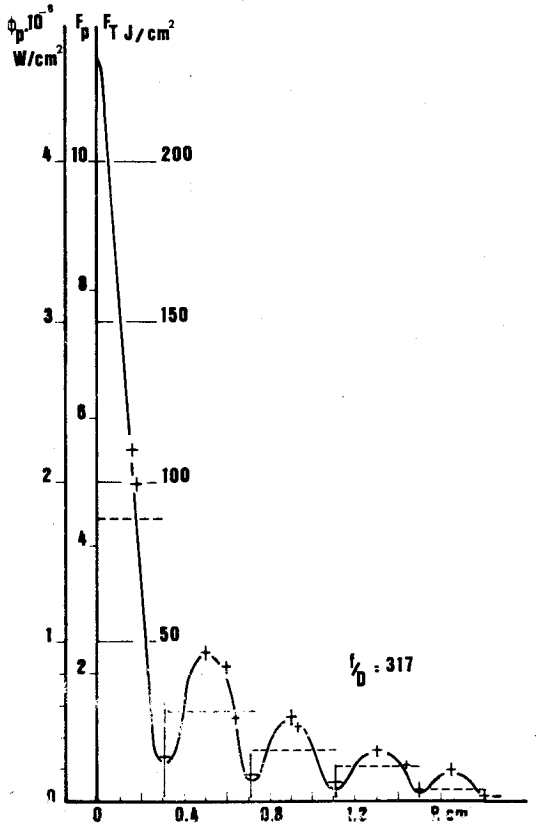

Fig. 7 Diffraction ring-structure energy density distribution at $f/D = 317$. Dashed lines are average values on each ring surface.

The energy located in each ring is given by the following formula:

$$E_T = \sum_{\text{rings}} \int_{S_{\text{ring}}} \int F_T \mathrm{d}S = \int_{t=0}^{t=2.5\mu s} W(t)\,\mathrm{d}t$$

where S_{ring} is the ring surface, F_T is the total fluence on each ring, R is the spot radius, and $W(t)$ is the laser pulse power (Fig. 5).

Note that in Table 2, for each focal length, the central lobe does not contain more than 20% of the incident energy while peak intensity remains very high. On the last line are plotted for comparison theoretical percentages of energy in each ring for an annular apertured diffraction limited beam free from spherical aberrations. (A theoretical computed investigation is being conducted to study linked effects of spherical aberration and diffraction on intensity pattern. This study takes into account the actual shape of the mirrors' surfaces.)

The aforementioned results, when related to the temporal power distribution of the laser pulse, lead to determination of spike fluence F_P and maximal intensity ϕ_P reached at $t = 50$ ns (Fig. 6); for example, $F_P = 62.7$ J/cm^2 and $\phi_P = 25 \times 10^8$ W/cm^2 at $f/D = 135$.

$$E_P = \sum_{\text{rings}} \int_{S_{\text{ring}}} \int F_P \mathrm{d}S = \int_{t=0}^{t=50\text{ ns}} W(t)\,\mathrm{d}t$$

Variation of pulse power during the rise time being considered linear ($W(t) = at$, $0 < t < 50$ ns), the spatial average intensity distribution $\phi(t)$ is given by

$$F(t) = \frac{E(t)}{S} = \int \frac{W(t)}{S}\,\mathrm{d}t = \frac{at^2}{2S} = > \phi(t) = \frac{2F(t)}{t}$$

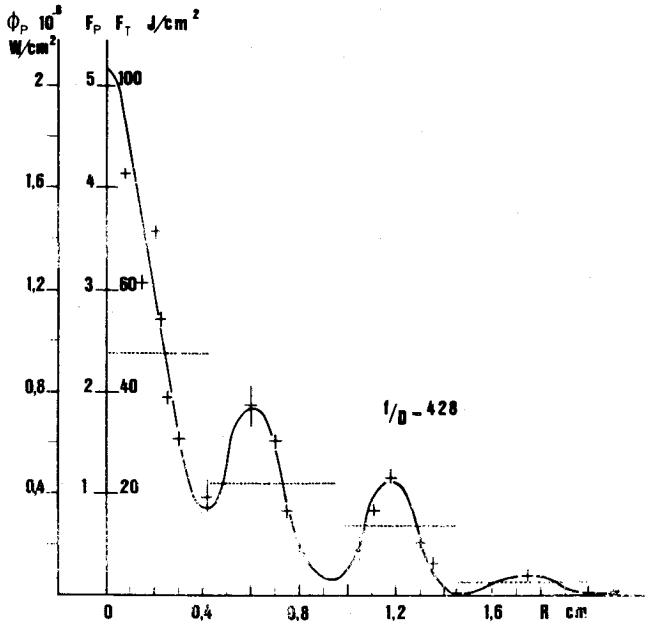

Fig. 8 Energy density distribution at $f/D = 428$. No breakdown was observed.

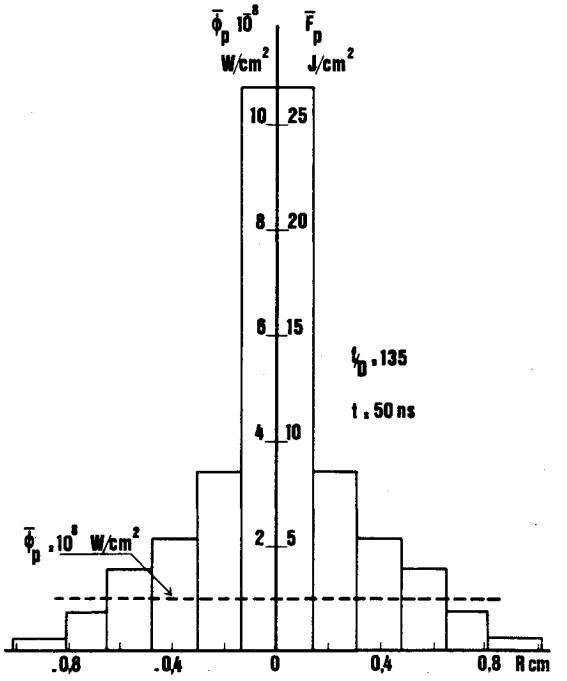

Fig. 9 Average fluence and intensity at $t = 50$ ns for $f/D = 135$.

Table 3 Intensity and fluence breakdown threshold values[a]

f/D	100% breakdown	Mylar attenuator factor	Central lobe area, $\times 10^{-2}$ cm^2	ϕ_s, $\times 10^8$ W/cm^2	$\bar{\phi}_s$, $\times 10^8$ W/cm^2	F_s, J/cm^2	$\bar{F}_s$, J/cm^2
135	Yes	8.4	6.15	3	1.3	7.4	3.2
	No	13		1.9	0.8	4.8	2.1
317	Yes	0	30.2	4.7	1.8	11.6	4.4
	No	1.53		3.1	1.2	7.6	2.9
428	Yes	...	55.4	...	...	...	...
	No	0		2.1	0.95	5.2	2.4

[a] Threshold intensity = $\phi_s = \phi_P$/mylar attenuation factor; threshold fluence = $F_s = F_P$/mylar attenuation factor; $\bar{\phi}_s$, $\bar{F}_s$ = spatial average values in the central lobe.

Average fluence $\bar{F}_P$ and average intensity $\bar{\phi}_P$ in each ring are also presented (Figs. 7-9) with

$$\underset{\text{ring } i}{\bar{F}_P} = \int_{S_{\text{ring } i}} \int F_P \mathrm{d}S \Big/ S_{\text{ring } i}$$

Figures 7 and 8 show the diffraction ring structure energy density distribution at $f/D = 317$ and 428 for a high-energy pulse. No breakdown was observed at $f/D = 428$. Dashed lines are average values on each ring surface. Figure 9 shows the average fluence and intensity at $t = 50$ ns for $f/D = 135$.

Determination of Threshold Fluence and Threshold Intensity Leading to Breakdown

The breakdown threshold is defined as the minimum intensity which produces light emission (spark). An investigation of the time of the air breakdown (light emission recorded by photodiode) shows that breakdown is initiated on the spike early in the pulse. For given optical configurations, the previously described laser pulse is attenuated by a range of mylar sheets ($I = I_0 e^{-kx}$, $k = 1.7 \times 10^{-2}$, $x = 25$ μm step thickness). It is then possible to determine, with an accuracy factor of 1.5, threshold values of intensity and fluence. The relative error on results is estimated to $\pm 10\%$.

Table 4 Experimental conditions for short-pulse experiments

f, m	D, m	f/D	Δt, ns	W_{max}, W	E, J
4	0.04	100	1	5×10^9	7.5

Intensity and fluence breakdown threshold values located in the central lobe are presented in Table 3. It should be noted that the spatial average threshold fluence $\bar{F}_S$ at $t = 50$ ns (obtained directly for Kalvar film measurements) necessary to generate air breakdown in our experimental conditions (0.28 cm < spot diameter < 0.88 cm) is close to 3-5 J/cm^2, while peak values of F_S are similar to those given by other authors (10 J/cm^2).[9-16]

Other threshold measurements were conducted with a 15 J laser pulse delivered by a CO_2 double-discharge high-power peak laser (10^{10} W with a rise time of a 1 ns on the ramping portion, 1.5 ns full width at half maximum). Experimental conditions for these short-pulse experiments are presented in Table 4.

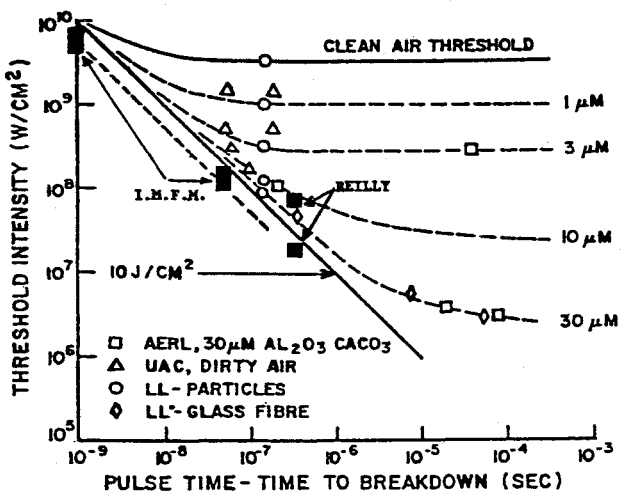

Fig. 10 (Lincoln Laboratory correlation of dirty air breakdown characteristics.[9]) Comparison of average fluence and intensity threshold values obtained for pulse length $\tau = 1$ and 50 ns with previously published results.[9-16] From Ref. 16, the upper square ($5\text{-}10 \times 10^7$ W/cm^2) represents the peak flux for which there are 100% breakdowns, the lower square ($1\text{-}2 \times 10^7$ W/cm^2) 0% breakdown.

The measured breakdown threshold intensity ($4\text{-}8 \times 10^9$ W/cm^2) is related to an average threshold fluence of 2-4 J/cm^2. Values of $\bar{F}_S$ for different pulse lengths are presented in Fig. 10 and compared to previous experimental results (Lencioni-Smith-Reilly). Those results are in agreement with precedent results (slightly lower) (from Fig. 5 of Ref. 9, $\phi_s = 2\text{-}2.6 \times 10^8$ W/cm^2 for 10 ≤ diameter ≤ 30 μm with 50 ns pulse length).

Values of $\bar{\phi}_s$ are similar to those previously measured[12] (dashed lines on Fig. 10). On the other hand, maximal values ϕ_s presented in this study are, of course, higher. Average threshold intensity remains nearly constant ($10^8 \leq \bar{\phi}_s \leq 2 \times 10^8$ W/cm^2) for large focal numbers ($f/D \geq 100$, i.e. diameter spot ≥ 0.2 cm).

According to Lencioni's work,[5,9] which states that the breakdown threshold is found to be extremely sensitive to the particles' size but not very much to their chemical composition (except for distilled water), it is possible to deduce that breakdown is induced by particles whose diameter is higher or equal to 4 μm (see Fig. 2 of Ref. 5).[¶]

Our experimental investigation consists of defining an elementary cone-shaped volume V in which breakdown is liable to occur first (threshold interaction volume) and then associating with it the probability that particles of given diameter will be present (aerosol distribution).

It is possible to establish an axial interaction length considering the variations of the maximum intensity $I(\Delta f, r)$ of the central lobe along the optical axis for an annular apertured beam:

$$\frac{I(\Delta f,0)}{I(0,0)} = \left\{ \sin\left[(1-\theta)^2 \frac{2\pi a^2}{\lambda} \frac{\Delta f}{4f^2}\right] \Big/ \left[(1-\theta)^2 \frac{2\pi a^2}{\lambda} \frac{\Delta f}{4f^2}\right] \right\}^2$$

where f is the focal length, Δf the distance from the focus, θ the internal and external beam diameters ratio ($d/D = 2/3$), and a the external beam radius at the output pupil of the telescope.

f is then chosen so that

$$\frac{I(\Delta f,0)}{I(0,0)} = \frac{1}{K}$$

with $K = 1.53$ (25 μm attenuating step).

The cone base radius r is determined, looking at Figs. 7-9:

$$\frac{I(0,r)}{I(0,0)} = \frac{1}{K}$$

This leads to the following formula for the elementary volume in which the breakdown first occurs:

$$V = 1.68\lambda^3 (f/D)^4$$

Values of V in experimental conditions are shown in Table 5.

Table 5 Elementary focal volume values

f/D	Δf,[a] m	V,[b] cm^3
135	0.97	0.66
317	5.3	20
428	9.8	67

[a] Δf = distance from the focus. [b] V = elementary focal volume.

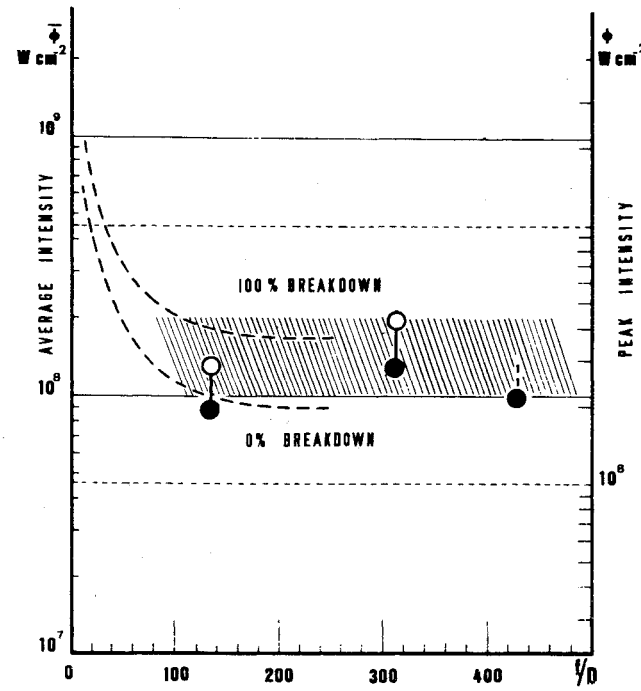

Fig. 11 Threshold intensity (peak and average values) as a function of f number of the optical system: • = 0% breakdown, ○ = 100% breakdown.

Aerosol Distribution

A particle optical counter is used for aerosol concentration and size distribution in situ measurements. Aerosols are generally composed of particles whose size may range from smaller than 0.01 μm (Aitken particles) to larger than 20 μm (giant particles). They display various chemical compositions and each of them can be a conglomerate of different materials according to geographical situation and meteorological conditions. The most suitable model for our laboratory location is a combination of rural (continental) and maritime models.[17]

[¶] Figure 2 of Ref. 5 gives breakdown thresholds vs particle size for various materials. From this figure, it is possible to estimate the diameter of particles for which the breakdown threshold is $1\text{-}2 \cdot 10^8$ W/cm^2, i.e., for particles ≥ 4 μm diameter. For example ϕ_s breakdown threshold (5 μm diameter) is ≃ $2 \cdot 10^8$ W/cm^2, ϕ_s breakdown threshold (50 μm diameter) is ≃ $5\text{-}8 \cdot 10^7$ W/cm^2. Then taking into account the measurements of aerosol concentration and size distribution in the atmosphere, it is possible to see that the probability of finding particles with diameter > 10 μm is very weak, in our focal volumes (Table 7). It is the reason for this conclusion: that breakdown is induced by 4-10 μm diameter particles.

Continental background is partly due to chemical reactions between various gases in the atmosphere and partly to suspended dust particles (70% water-soluble substances such as NH_3, SO_4, and organic compounds, and 30% dust). Their concentration may be largely dependent on the history of the airmass which carry them.

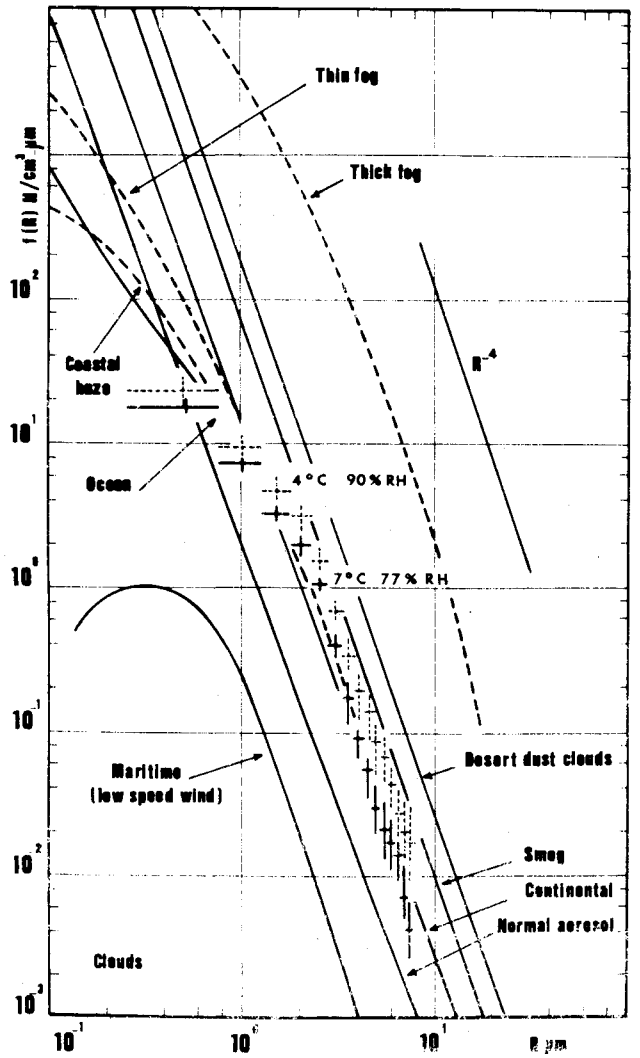

Fig. 12 Environmental aerosol distribution.

Table 6 Meteorological conditions

Temp., °C	Relative humidity, %	Specific humidity, g(H_2O)/m^3 (dry air)	Saturation value, g/m^3
+ 4	90	4.6	5.1
+ 7	78	5	6.3

The maritime model shows solid salt particles generated after evaporation or extraction of water droplets from the sea surface. The most common components are cations such as NA, K, Ca, and Mg with weight ratios of 83%, 10%, 3.3%, and 3.3%, respectively.[18] The number of seaspray-produced aerosols increase (especially the largest of them) with windspeed. Their size distribution is a function of relative humidity since hydroscopic particles grow by absorption of water when relative humidity goes over 30-40%.[19]

The particle optical counter used during experimental work (Knollenberg Axially Scattering Spectrometer Probe (ASSP) 100 calibrated in the 0.5-45 μm diam range)[20] displays the number and size of particles crossing an He-Ne focused laser beam by means of a photodiode which measures scattered light intensity:

$$I = I_0 F(n, \theta, \lambda, D, \alpha)$$

where n is the refractive index of the particle, θ the observation cone angle, $\lambda = 6328$ Å, and $\alpha = \pi D/\lambda$ where D is the particle diameter.

The electrical information given by the probe is amplified according to the chosen diameter range (0.5-7.5 μm, 1-15 μm, 2-30 μm, 3-45 μm) and each range is then equally divided into 15 linear size intervals.

The characteristics of utilization are:

Maximal count frequency = 10^5 particles/s
Coincidence error = < 1% with concentration of 10^3/cm^3
Sample area $S = 0.4$ mm^2
Particle flow speed ≃ 10-125 m/s
Temperature = −40 to +40°C
Relative humidity = 0-100%
Altitude = 0-13 km

The measurements assume that the particles are ideal spheres, which is true when the humidity is greater than 30-40%. Under other conditions, measurement accuracy decreases and correction ratios should be used.

Figure 12 shows environmental aerosol distribution during breakdown measurements, that is, for the meteorological conditions shown in Table 6.

These results can be compared to characteristic distributions of liquid and solid aerosols for different meteorological conditions and at ground level (see Figs. 2.1 and 2.2 of Ref. 21).

These measurements are in agreement with a continental aerosol distribution which can be represented by the function[21]

$$f(r) \simeq f_0 (r_1/r)^N = 10^6 (10^{-1}/r)^4 \qquad \text{particles} \cdot \text{cm}^{-3} \cdot \mu\text{m}^{-1}$$

In the range measured by the particle optical counter ($1 \le d \le 15$ μm) (Fig. 12), results can be represented by

$$f(r) \simeq 20(1.12/r)^4 \qquad \text{particles} \cdot \text{cm}^{-3} \cdot \mu\text{m}^{-1}$$

Table 7 presents the estimated number of particles larger than the critical diameter d^* (4 μm, 10 μm, 20 μm), (obtained from Fig. 2.5 of Ref. 21), that are liable to be situated in each previously defined elementary volume.

Table 7 Number of particles in the elementary focal volume[a]

	Particles/cm^3		Particles in the elementary volume V		
d^*, μm	$d = d^*$	$d > d^*$	$f/D = 135$ $V = 0.66$ cm^3	$f/D = 317$ $V = 20$ cm^3	$f/D = 428$ $V = 67$ cm^3
4	2.5	3.5	2.3	70	235
10	0.06	0.16	0.1	3.2	10.7
20	...	0.025	0.02	0.5	1.6

[a] The first column on the left gives the critical diameter d^* of the active aerosols liable to product air breakdown; the second gives the number of the aerosols with $d = d^*$ (experimental values shown in Fig. 12); the third gives the total number of particles the diameter of which is greater than the critical diameter d^* (from Fig. 2.5 of Ref. 21).

Conclusion

Considering laser pulse shape and duration, this independent experimental confirmation of the well-known result regarding aerosol-induced breakdown threshold shows that propagation through the standard atmosphere is possible for average intensity and fluence values up to $1\text{-}2\times10^8$ W/cm^2 and 3-5 J/cm^2, respectively.

Aerosol concentration and aerosol size distribution measurements lead to the conclusion that air breakdown is induced by 4-10 μm diam particles.

One possible way of propagating laser beams of greater intensity and fluence through the standard atmosphere is to pre-clean the beam path by means of a precursor pulse. The latter could vaporize, break up, or eject particles out of the focal volume.

Acknowledgments

We would like to thank J. P. Fragassi for his assistance throughout the course of this work. This work is sponsored by Direction des Recherches, Etudes et Techniques.

References

[1] Smith, D. C., "Gas-Breakdown Dependence on Beam Size and Pulse Duration with 10.6 μm Wavelength Radiation," *Applied Physics Letters,* Vol. 19, Nov. 1971, pp. 405-408.

[2] Marquet, L. C., Hull, R. J., and Lencioni, D. E., "Studies of Breakdown in Air Induced by a Pulsed CO_2 Laser," *IEEE Journal of Quantum Electronics,* Vol. QE8, June 1972, pp. 564.

[3] Kroll, N. and Watson, K. M., "Theoretical Study of Ionization of Air by Intense Laser Pulses," *Physical Review,* Vol. A5, April 1972, pp. 1833-1905.

[4] Canavan, G. H. and Nielsen, P. E., "Focal Spot Size Dependence of Gas Breakdown Induced by Particulate Ionization," *Applied Physics Letters,* Vol. 22, April 1973, pp. 409-410.

[5] Lencioni, D. E., "The Effect of Dust on 10.6 μm Laser Induced Air Breakdown," *Applied Physics Letters,* Vol. 23, July 1973, pp. 12-14.

[6] Lowder, J. E. and Kleiman, H., "Long-Pulse Breakdown with 10.6 μm Laser Radiation," *Journal of Applied Physics,* Vol. 44, Dec. 1973, pp. 5504-5505.

[7] Lencioni, D. E., "Laser-Induced Air Breakdown for 1.06 μm Radiation," *Applied Physics Letters,* Vol. 25, July 1974, pp. 15-17.

[8] Smith, D. C. and Brown, R. T., "Aerosol-Induced Air Breakdown with CO_2 Laser Radiation," *Journal of Applied Physics,* Vol. 46, March 1975, pp. 1146-1154.

[9] Lencioni, D. E., "The Limitations Imposed by Atmospheric Breakdown on the Propagation of High Power Laser Beams," *AGARD Conference Proceedings,* No. 183, Oct. 1975, pp. 32.1-32.12.

[10] Lencioni, D. E. and Pettingill, L. C., "The Dynamics of Air Breakdown Initiated by a Particle in a Laser Beam," *Journal of Applied Physics,* Vol. 48, May 1977, pp. 1848-1851.

[11] Smith, D. C., "Gas Breakdown Initiated by Laser Radiation Interaction with Aerosols and Solid Surfaces," *Journal of Applied Physics,* Vol. 48, June 1977, pp. 2217-2225.

[12] Autric, M., Caressa, J. P., Dufresne, D., and Bournot, Ph., "Laser-Induced Air Breakdown for 10.6 μm Radiation," AIAA Paper 79-0250, Jan. 1979.

[13] Caressa, J. P., Autric, M., Dufresne, D., and Bournot, Ph., "Experimental Study of CO_2-Laser-Induced Air Breakdown over Long Distances," *Journal of Applied Physics,* Vol. 50, Nov. 1979, pp. 6822-6825.

[14] Klingler, Q. G., "Spatial Laser Diagnostics and Development of Kalvar Film," Los Alamos Operations, 1975.

[15] Manning, J. and Klingler, Q. G., Kalvar Film Report, Los Alamos Operations, LAO 196, Oct. 1974.

[16] Reilly, J. P., Singh, P., and Weyl, G., "Multiple Pulse Laser Propagation through Atmospheric Dusts at 10.6 Microns," AIAA Paper 77-697, June 1977.

[17] Shettle, E. P. and Fenn, R. W., "Models of the Atmospheric Aerosols and Their Optical Properties," *AGARD Conference Proceedings,* No. 183, Oct.1975, pp. 2-1 to 2-16.

[18] Morelli, J., "Données sur le cycle atmosphérique des sels marins," *Journal de Recherches Oceanographiques,* Vol. III, 1978, pp. 27-49.

[19] Winkler, P., "On Production Rates in Marine Aerosols," *Proceedings of the Symposium on Radiation in the Atmosphere,* Science Press, Garmish, Aug. 1976, pp. 50-53.

[20] Soulage, R. G., Laboratoire Associé de Météorologie Physique, Université Clermont II.

[21] Reilly, J. P., Delichatsios, M., Glickler, S. L., Korff, D., Singh, P. I., and Weyl, G. M., "Multiple Pulse Propagation in Fog, Rain and Dust at 10.6 μm," AVCO Everett Research Labs., Interim Report, 173-76C 0059, July 1976.

[22] Lencioni, D. E. and Lowder, J. E., "Aerosol Clearing with a 10.6 μm Precursor Pulse," *IEEE Journal of Quantum Electronics,* Vol. QE 10, 1974, pp. 235-238.